Spontaneous anterior-posterior convergences of oscillation frequencies in the alpha band

Satoru Suzuki[1,2*], Marcia Grabowecky[1,2], Melisa Menceloglu[1,#a]

[1]Department of Psychology, Northwestern university, Evanston, IL, U.S.A

[2]Interdepartmental Neuroscience, Northwestern university, Evanston, IL, U.S.A

[#a]Cognitive, Linguistic, and Psychological Sciences, Brown university, Providence, RI, U.S.A

* Corresponding author

Email: satoru@northwestern.edu (SS)

Abstract

Peak alpha frequencies vary along the anterior-posterior axis, but they also dynamically converge. We investigated such spontaneous anterior-posterior oscillation-frequency convergences by tracking oscillatory EEG activity in an extended alpha range (5-15 Hz) with appropriate temporal (~370 ms) and spectral (~1 Hz) resolutions. Our analysis revealed three primary characteristics. First, the probability of an additional site joining a frequency convergence increased as more sites frequency-converged, suggesting that anterior-posterior frequency convergences are driven by synergistic interactions. Second, the oscillatory power at participating sites increased as more sites frequency-converged, suggesting that the synergistic interactions are mediated by regional synchronizations, being boosted by inter-regional frequency matching, facilitating the entrainment of additional regions. Third, frequency convergences generated two opposing phase gradients, posterior-behind and posterior-ahead (while tending to plateau from central to anterior sites), potentially mediating directional information flows to and from posterior cortex. These gradients became steeper as more sites frequency-converged (while maintaining relatively constant levels of phase consistency), suggesting that frequency convergences increase the directionality of anterior-posterior information flows. Interestingly, when participants rested with their eyes closed (but not when they viewed a silent nature video), the opposing phase gradients spatially segregated, forming posterior-behind gradients within each hemisphere and posterior-ahead gradients along the midline, suggesting that closing eyes tightens the organization of directional information flows to and from posterior cortex. These results primarily reflected alpha-band activity (8-13 Hz) where oscillation-frequency convergences were prominent. Taken together, our results suggest that spontaneous anterior-posterior oscillation-frequency convergences in the alpha band are synergistically driven and may contribute to directional flows of oscillatory information to and from posterior cortex.

Introduction

Oscillatory neural activity is prevalent in the brain [e.g., 1]. In particular, inter-regional phase locking of oscillatory activity has been proposed to play a crucial role in controlling neural communications [e.g., 2-3], spurring much research examining inter-regional phase coherence within and between frequency bands. Most studies measured phase coherence as a period of stable phase difference, $\Delta\phi(t) = n\phi_A(t) - m\phi_B(t) \sim constant$, between signals from a pair of brain regions A and B at frequencies of a ratio, $m{:}n$ (where $\phi_A(t)$ and $\phi_B(t)$ are instantaneous phases at regions A and B obtained by Hilbert transforming band-passed signals, convolving with Morlet wavelets, etc.). For example, one would set $m = n = 1$ for examining within-frequency phase coherence, $m = 1$ and $n = 3$ for examining cross-frequency phase coherence between f and $3{\times}f$, and so on. Those studies primarily focused on identifying frequency-specific functional networks organized by within- and/or cross-frequency phase coherence in specific frequency bands. Extensive research using this approach has identified a variety of frequency-specific functional networks and elucidated how they contribute to perceptual, attentional, and cognitive processes [e.g., 4-7].

Focusing on phase coherence in band-passed signals, however, obscures the fact that oscillation frequencies generally differ across brain regions [e.g., 8-9] and they fluctuate over time [e.g., 10-11]. In order for a pair of regions to stably interact through oscillatory phase locking, their oscillation frequencies need to converge (to the same frequency for within-frequency oscillatory interactions, which was the focus of the current study, or to frequencies of a ratio, $m{:}n$, for cross-frequency oscillatory interactions). Thus, a complementary approach to examining inter-regional oscillatory interactions is to track oscillation frequencies in multiple regions and examine how they dynamically converge. Oscillation frequencies in each region (e.g., an intracranial electrode, EEG/MEG scalp site, inferred source, etc.) can be tracked by applying time-frequency decomposition (e.g., using Morlet wavelets) with appropriate spectral and temporal resolutions, then tracking spectral-power ridges (or stationary-phase points where $\frac{dPhase}{dt} = 2\pi f$) as a function of time [e.g., 12-14]. Using this method, previous studies examined spontaneous inter-regional oscillation-frequency convergences in pre-seizure neural activity [e.g., 12-13] as well as frequency convergences to consciously perceived visual flicker during binocular rivalry using frequency-tagged stimuli [13].

Our goal here was to uncover macroscopic rules governing spontaneous inter-regional oscillation-frequency convergences during rest using scalp-recorded EEG. Do macroscopic oscillation-frequency convergences occur by coincidence or are they driven? If driven, what

mechanisms propel oscillation frequencies in different regions to converge? What functions might inter-regional oscillation-frequency convergences serve? We sought clues to answering these questions by examining the spreading of oscillation-frequency convergences in relation to oscillatory power and phase relations.

We focused on oscillation-frequency convergences along the anterior-posterior axis partly because neural communications between anterior and posterior brain regions have been implicated in a variety of perceptual, attentional, and cognitive processes [e.g., 6-7,15-18] and partly because consistent anterior-posterior gradients of neuroanatomical and neurophysiological features have been reported including neuron density, myelination, cortical density, functional-connectivity patterns, temporal integration, and oscillation frequency [e.g., 9,19-20]. We tracked oscillation frequencies in an extended alpha range (5-15 Hz) because they have been implicated in a variety of perceptual, attentional, and memory processes [e.g., 3,6,17,21-26], have been shown to influence gamma-band activity [e.g., 27-28], and may organize information flows [e.g., 29-31].

We examined the dynamics of spontaneous anterior-posterior oscillation-frequency convergences in the extended alpha range (5-15 Hz) in three representative rest conditions, while participants (1) rested with their eyes closed, (2) rested with their eyes open in a dark room, or (3) viewed a silent nature video. We examined the probabilistic, power, and phase characteristics of inter-regional oscillation-frequency convergences to infer their potential mechanism and function. With regard to their potential mechanism, our results suggest that inter-regional oscillation-frequency convergences are driven by synergistic interactions wherein regional synchronizations boosted by inter-regional frequency matching facilitate the entrainment of additional regions. With regard to their potential function, our results suggest that inter-regional oscillation-frequency convergences generate opposing anterior-posterior phase gradients that may facilitate directional information flows to and from posterior cortex. Interestingly, when eyes were closed, these gradients spatially segregated, posterior-ahead gradients occurring along the midline and posterior-behind gradients occurring within each hemisphere.

Materials and methods

Participants

Fifty-two Northwestern University students (35 women, 1 non-binary; mean age of 20.8 years, ranging from 18 to 29 years, standard deviation of 2.5 years) gave informed written consent to participate for monetary compensation ($10/hour). All participants were right-handed, had normal hearing and normal or corrected-to-normal vision, and had no history of concussion. They were tested individually in a dimly lit or darkened room. The study protocol was approved by the Northwestern University Institutional Review Board. A group of twenty-four individuals participated in a rest-with-eyes-closed condition in which EEG was recorded for ~5 min while participants rested with their eyes closed and freely engaged in spontaneous thoughts. A second (non-overlapping) group of twenty-four individuals participated in a replication of the rest-with-eyes-closed condition and subsequently participated in a rest-with-eyes-open-in-the-dark condition which was the same as the former except that the room was darkened and participants kept their eyes open while blinking naturally. A third group of twenty-one individuals (seventeen of whom previously participated in the rest-with-eyes-closed condition) participated in a silent-nature-video condition in which EEG was recorded for ~5 min while they viewed a silent nature video. To evaluate test-retest reliability, the silent-nature-video condition was run twice (20-30 min apart), labeled as earlier viewing and later viewing in the figures. A generic nature video was presented on a 13-inch, 2017 MacBook Pro 2880(H)-by-1800(V)-pixel-resolution LCD monitor with normal brightness and contrast settings, placed 100 cm in front of participants, subtending approximately 16° (H)-by-10° (V) of visual angle. Subsets of these data were previously analyzed for different purposes [32-36].

EEG recording and pre-processing

EEG was recorded from 64 scalp electrodes (although we used a 64-electrode montage, we excluded signals from noise-prone electrodes, Fpz, Iz, T9, and T10, from analyses) at a sampling rate of 512 Hz using BioSemi ActiveTwo system (see www.biosemi.com for details), while participants rested with their eyes closed, rested with their eyes open in the dark, or viewed a silent nature video for approximately 5 min. Electrooculographic (EOG) activity was monitored using four face electrodes, one placed lateral to each eye and one placed beneath each eye. Two additional electrodes were placed on the left and right mastoids. The EEG data were preprocessed using EEGLAB and ERPLAB toolboxes for MATLAB [37-38]. The data were

re-referenced offline to the average of the two mastoid electrodes and high-pass filtered at 0.01 Hz to remove drifts.

Estimating dura sources by surface-Laplacian transforming EEG signals

EEG source reconstruction methods constrained by structural MRI and fMRI localizers obtained from each participant can achieve superior source reconstruction with a brain model customized for each participant [39]. However, such approach was unavailable to us as we had neither structural MRI nor fMRI data for our participants. Among the non-customized source-imaging methods, we chose the surface-Laplacian transform that (theoretically) estimates the spatial distribution of macroscopic current sources and sinks at the dura surface. The surface-Laplacian transform has been shown to produce similar sources to those inferred by deconvolving scalp potentials using a generic model of thicknesses and impedances of scalp and skull [40]. The surface-Laplacian transform has also been shown to approximate simulated sources and/or to extract neural correlates of some behavioral performances to a similar degree to commonly used source-imaging methods such as sLORETA and Beamforming [41-42]. Further, there is no evidence (to our knowledge) to suggest that the latter source-imaging methods provide greater spatial resolution than the surface-Laplacian transform. Thus, our preference was to use the surface-Laplacian transform which is the most general source-imaging method that relies the least on model-specific assumptions and free parameters [40-41,43-45].

The surface-Laplacian transform is expected to reduce volume-conduction effects from substantially greater than 5 cm in raw EEG to within 1-3 cm [36,40-41,46] which approximately corresponded to the average spacing of electrodes in our 64-channel montage. For our implementation of the surface-Laplacian transform, we used Perrin and colleagues' algorithm [47-49] with a "smoothness" value, $\lambda = 10^{-5}$ (recommended for 64 channels [46]). We refer to the surface-Laplacian transformed EEG signals that represent the macroscopic current sources and sinks on the dura surface under the 60 scalp sites (with the 4 noise-prone sites excluded from the analyses) simply as EEG signals.

EEG analysis

Taking the temporal derivative. Our goal was to track spectral maxima (likely indicative of oscillation frequencies) at sub-second temporal resolution. The general $1/f^{\beta}$ spectral background in EEG interferes with the identification of spectral maxima. A commonly employed strategy to circumvent this problem is to compute a Fourier transform over partially overlapping

time windows of several seconds or longer, and then fit a power function to each time-windowed Fourier transform to subtract out the $1/f^{\beta}$ component [e.g., 50-52]. However, it is difficult to reliably estimate the $1/f^{\beta}$ component on a sub-second timescale. Note that β in the $1/f^{\beta}$ spectral background varies around 1 (see [53] for a review of the various factors that influence β, and [54] for contributions of the excitatory and inhibitory neural dynamics to β). Although taking the temporal derivative of EEG ($\frac{\Delta EEG}{\Delta t}$, where Δt is the temporal resolution, i.e., 1/512 sec here) would completely neutralize the $1/f^{\beta}$ component only when $\beta = 1$, the method worked well for our data [32,34-36], suggesting that $\beta \sim 1$ generally held for our data. As we discussed in our prior reports [34-36], taking EEG temporal derivative offers additional advantages. For example, EEG temporal derivatives are drift free. Further, EEG temporal derivatives may be considered a deeper measure of neural activity than EEG in the sense that scalp-recorded potentials are generated by the underlying neural currents and taking EEG temporal derivative macroscopically estimates those currents (as currents in an RC circuit are proportional to the temporal derivative of the corresponding potentials). There is some evidence that EEG temporal derivatives offer a more effective neural measure than EEG for brain-computer interface [55].

Time-frequency decomposition using Morlet wavelets. To track EEG power spectra at high temporal and spectral resolutions, we used a Morlet wavelet-convolution method suitable for time-frequency decomposition of signals containing multiple oscillatory sources of different frequencies (see [46] for a review of different methods for time-frequency decomposition). Each Morlet wavelet is a Gaussian-windowed complex sinusoidal template characterized by its frequency as well as its temporal and spectral widths that limit its temporal and spectral resolutions. We convolved each EEG waveform (i.e., its temporal derivative) with a set of wavelets tuned to a range of frequencies, yielding a time series of complex values per wavelet frequency. The power and phase of each extracted sinusoidal component at each time point were given by the modulus squared (power) and the arc tangent of the ratio of the imaginary component to the real component (phase). We used a set of wavelets with 160 frequencies, f_w's, ranging from 5 Hz to 15 Hz. The f_w's were logarithmically spaced as neural temporal-frequency tunings tend to be approximately logarithmically scaled [56-57]. The accompanying n factor (roughly the number of cycles per wavelet, with the precise definition, $n = 2\pi f \cdot SD$, where SD is the wavelet standard deviation) was also logarithmically spaced between 11.7 and 35. This spacing yielded a temporal resolution of $SD = 370$ ms and a spectral resolution of, $FWHM\ (full\ width\ at\ half\ maximum\ of\ wavelet\ spectrum) = 1.0$ Hz, that were virtually invariant across the wavelet frequencies.

Identifying oscillation frequencies per time point. When multiple oscillations at neighboring frequencies coincide, each oscillation frequency does not necessarily generate a local maximum in the power spectrum due to a limited spectral resolution. An example is shown in Fig 1A, plotting a single-time-point power spectrum obtained with our Morlet wavelets for a simulated data containing five sinusoidal oscillations at 6, 7, 9.5, 10.5, and 13 Hz (vertical arrows) of differing amplitudes. Oscillation frequencies are typically identified as spectral peaks that theoretically coincide with the points of phase stationarity [e.g., 14]. However, only three of the five oscillation frequencies were identified as spectral peaks (black open circles in Fig 1A) which coincided with the points of phase stationarity (negatively sloped zero crossings of $\frac{dPhase}{dt} - 2\pi f$ in Fig 1B). Spectral peaks and phase stationarity missed the low-amplitude oscillations at 7 Hz and 9.5 Hz in the neighborhoods of the high-amplitude oscillations at 6 Hz and 10.5 Hz (Fig 1A).

We thus used a more sensitive method to identify oscillation frequencies. As shown in Fig 1C, our wavelet-based time-frequency decomposition generated Gaussian-shaped power spectra for single-frequency oscillations (point-spread functions). We took advantage of the fact that the curvature of a Gaussian function (maximum at its peak) falls faster than its value. Thus, local curvature maxima provide a higher spectral resolution for identifying oscillation frequencies than spectral peaks. For example, the low-amplitude oscillations at 7 Hz and 9.5 Hz generated curvature maxima (red open circles in Fig 1A) though they did not generate spectral peaks (or points of phase stationarity). We tracked curvature maxima as a function of time at anterior-posterior sites along the midline (AFz, Fz, FCz, Cz, CPz, Pz, POz, and Oz) as well as in the left (AF3, F3, FC3, C3, CP3, P3, PO3, and O1) and right (AF4, F4, FC4, C4, CP4, P4, PO4, and O2) hemispheres.

The number of identified curvature maxima per time point was consistent across participants and behavioral conditions, showing nearly identical distributions centered around eight (Fig 2). It is likely that some of these curvature maxima were due to noise. Nevertheless, instead of imposing an arbitrary power threshold, we analyzed our data relative to their time-shuffled controls as described below. Spurious effects due to noise would be statistically equivalent for the actual data and their time-shuffled controls.

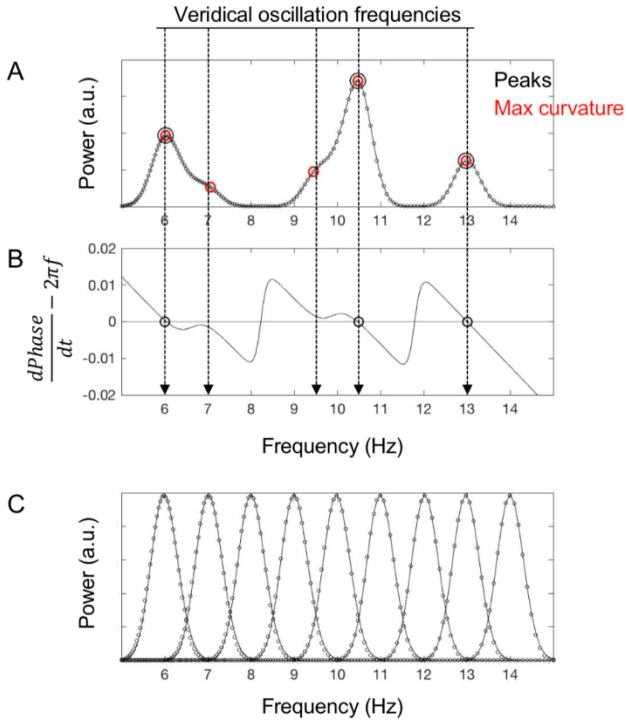

Fig 1. Identifying oscillation frequencies as curvature maxima in a power spectrum (per time point). A. A single-time-point power spectrum of simulated EEG data containing sinusoidal oscillations at 6, 7, 9.5, 10.5, and 13 Hz (vertical arrows) of various amplitudes, processed with our 160 wavelets (see text). The black open circles indicate oscillation frequencies identified as spectral peaks, whereas the red open circles indicate oscillation frequencies identified as curvature maxima. Note that only curvature maxima identified the low-amplitude oscillations at 7 Hz and 9.5 Hz occurring near the high-amplitude oscillations at 6 Hz and 10.5 Hz. **B.** A plot of $\frac{dPhase}{dt} - 2\pi f$ as a function of f (frequency). The negatively sloped zero crossings (black open circles) indicate the points of phase stationarity, which coincide with the spectral peaks. **C.** Representative point-spread functions (power spectra of single sinusoidal oscillations) showing the spectral resolution of our 160-wavlet spectral decomposition. They are well fit by Gaussian functions (continuous curves).

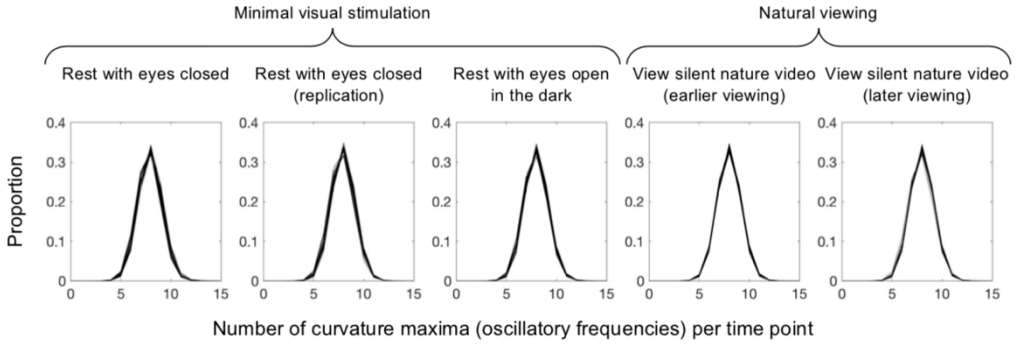

Fig 2. Distributions of the number of curvature maxima (oscillation frequencies) per time point for the five behavioral conditions. The distributions were averaged across all sites as they did not appreciably differ across sites. Each curve represents the average distribution from a single participant in the corresponding condition. Note that the distributions were similar across all participants and behavioral conditions.

Results

Our goal was to uncover general rules governing spontaneous oscillation-frequency convergences across anterior-posterior sites along the midline and in the left and right hemispheres. Extensive oscillation-frequency convergences involving nearly all eight anterior-posterior sites were rare when we required exact alignments of oscillation frequencies across sites. We thus registered oscillation-frequency convergences with a tolerance commensurate with the spacing of our 160 wavelet frequencies. Specifically, we broadened each identified oscillation frequency at each site (at each time point) by ±1 unit of our wavelet-frequency spacing, which logarithmically increased from ±0.04 Hz at 5 Hz to ±0.11 Hz at 15 Hz due to our logarithmic spacing of the 160 wavelet frequencies (see Materials and method). That is, we considered oscillation frequencies to be convergent when they were within ±0.04 Hz at the lowest end and within ±0.11 Hz at the highest end.

For each site (for each participant), we represented the temporal flows of oscillation frequencies in a wavelet-frequency-(row)-by-time-(column) matrix—the *flow matrix*. To implement the above-mentioned tolerance for frequency-convergence detection, each identified oscillation frequency at each time point as well as the frequency values immediately above and below it were given the value of 1, with the rest of the matrix filled with zeros. The temporal flows of spontaneous oscillation-frequency convergences were then obtained by stacking the flow matrices from the eight anterior-posterior sites on top of one another and summing them across the vertical dimension, yielding a wavelet-frequency-(row)-by-time-(column) matrix where values of 1 through 8 represented oscillation-frequency convergences across 1 through 8 sites. We call this the *flow-convergence matrix*.

How oscillation frequencies dynamically converged across anterior-posterior sites can be visualized by plotting a flow-convergence matrix. An example is shown in Fig 3 for one participant in the rest-with-eyes-closed condition where cooler/darker colors indicate frequency convergences across larger numbers of midline anterior-posterior sites. Our goal was to uncover general characteristics of these spontaneous oscillation-frequency convergences to infer their mechanism and function.

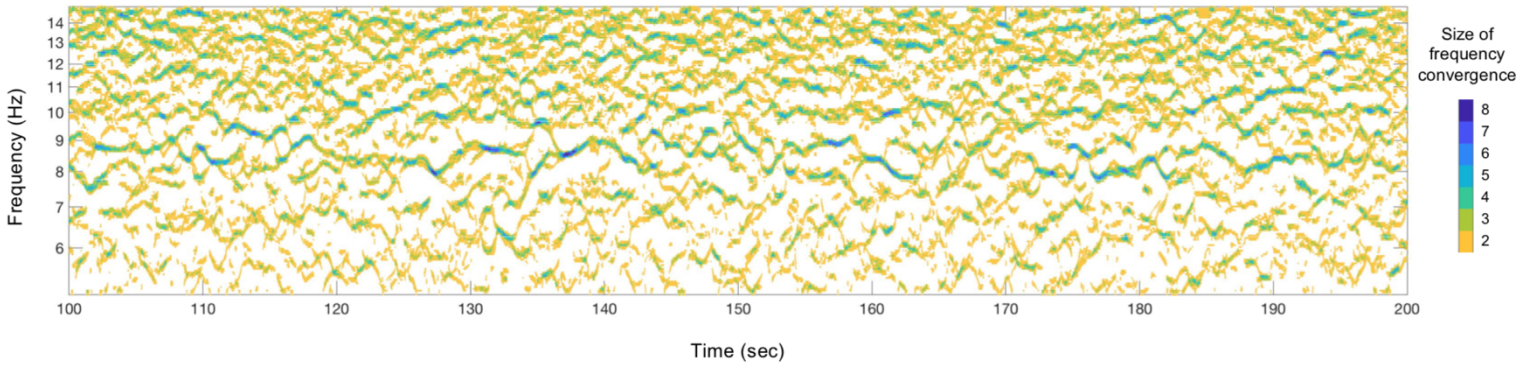

Fig 3. An example of oscillation-frequency convergences across the eight anterior-posterior sites along the midline as a function of time for one participant in the rest-with-eyes-closed condition during a 100-sec period. Cooler/darker colors indicate oscillation-frequency convergences across larger numbers of sites.

We first verified that spontaneous oscillation-frequency convergences were driven. As oscillations in the extended alpha range may contain dominant frequencies (e.g., ~10 Hz peaks), spontaneous frequency convergences might simply reflect coincidences of dominant oscillations across sites. The method we used to rule out this possibility was to compare the total durations of oscillation-frequency convergences of 1 through 8 sites between the actual flow-convergence matrices and their time-shuffled controls. We generated a time-shuffled version by randomly time-shifting the flow matrices of each site by up to 150 sec (a half of the total duration of ~5 min) prior to summing across those matrices. If the instances of oscillation-frequency convergences were due to coincidences, the total durations of frequency convergences should be equivalent for the actual and time-shuffled flow-convergence matrices. Total durations of frequency convergences across 1 through 8 sites can be approximately computed by tallying the total instances of 1's through 8's in a flow-convergence matrix. These values overestimated the actual total durations by up to three-fold as we broadened each oscillation-frequency flow by ±1 wavelet-frequency spacing to increase the tolerance of convergence detection (see above). Nevertheless, this was not problematic as we compared the actual total durations with those averaged from 20 time-shuffled controls (per behavioral condition per participant), given that total durations of convergences across 1 through 8 sites were computed in the same way for the actual and time-shuffled flow-convergence matrices.

As shown in Fig 4, the total durations of convergences of 4 or more sites were consistently elevated in the actual data (red curves) relative to the time-shuffled controls (black curves) for all participants in all behavioral conditions. Given that the total durations are plotted in log scale, these elevations were substantial.

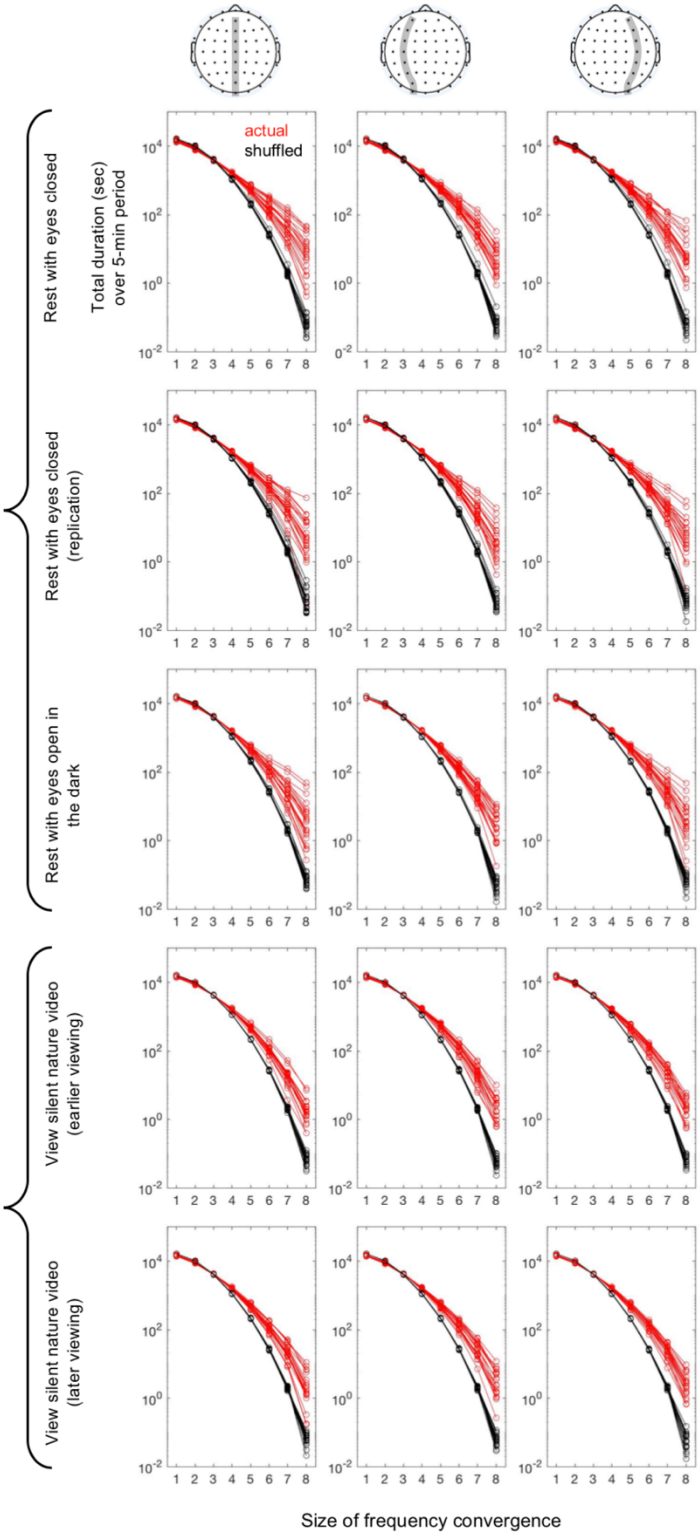

Fig 4. Approximate (see text) total durations (sec) of anterior-posterior oscillation-frequency convergences as a function of the size of frequency convergence, along the midline (first column) and in the left (second column) and right (third column) hemispheres, for the actual data (red) and time-shuffled controls (black, averaged across 20 versions) for the five behavioral conditions (rows). Each curve represents a participant. Durations of convergences of 4 or more sites were elevated in the actual data (red) relative to the time-shuffled controls (black) for all participants in all conditions.

Having verified that oscillation-frequency convergences were likely driven (rather than coincidences), we examined general characteristics of anterior-posterior oscillation-frequency convergences. While a variety of spatial, spectral, and temporal features of oscillation-frequency convergences can be investigated, we primarily focused on the following three questions. First, how are large oscillation-frequency convergences driven? Second, how are oscillation-frequency convergences related to oscillatory power? Third, do oscillation-frequency convergences generate consistent anterior-posterior phase relations? As discussed below, investigating these questions provided some insights into a potential mechanism and function of anterior-posterior oscillation-frequency convergences.

What mechanism may facilitate the spreading of anterior-posterior oscillation-frequency convergences? We reasoned that if oscillation-frequency convergences were driven by synergistic interactions, the propensity to converge would become stronger as more sites converged. We assessed this possibility by computing the probability of growing in convergence as a function of the number of converged sites. Using the flow matrix for each site (containing 1's where oscillations were identified, broadened by ±1 wavelet-frequency spacing; see above), we computed the average probability of frequency convergence across k sites. We first obtained the average base probability of oscillatory activity by computing the proportion of 1's in the flow matrix of each site and averaging the values across all sites. We call this $P(1)$, the average probability of oscillatory activity. If oscillation-frequency convergences were due to coincidences, the average probability of frequency convergences across k sites, $P(k)$, should be given by $P(1)^k$.

We computed the probability of frequency convergences across $k > 1$ sites as follows. For each combination of k sites, we stacked and summed their flow matrices and then computed the proportion of k's in the resultant matrix to obtain the probability of k convergence. We then averaged the probabilities computed for all combinations of k sites to obtain the average probability of k convergence, $P(k)$. To estimate the probability of growing in frequency convergence at each level of convergence (k), we computed the conditional probability of obtaining k convergence given $k-1$ convergence, $P(k|k-1)$, by dividing $P(k)$ by $P(k-1)$ because k convergence was a subset of $k-1$ convergence. We computed $P(k|k-1)$ (where $2 \leq k \leq 8$) for each participant for each behavioral condition.

As shown in Fig 5A, in all five behavioral conditions (rest with eyes closed, its replication, rest with eyes open in the dark, and the two instances of viewing a silent nature video) the probability of growing in convergence, $P(k|k-1)$, substantially increased as a function of the number of frequency-converged sites, k (red curves). Slight increases were also observed in

the time-shuffled controls (based on averaging 20 time-shuffled data) (black curves), indicating that some features of the flow matrices such as major oscillation flows occurring in relatively narrow frequency ranges slightly increased the probability of coincidental convergences relative to the chance level (gray lines). The data for the high frequency convergences (for $k = 7$ and especially for $k = 8$) were somewhat noisy as their instances were relatively rare especially for the time-shuffled controls (Fig 4). Importantly, $P(k|k-1)$ for the actual data generally increased more steeply than the time-shuffled controls as a function of k (Fig 5B). This indicates that the probability of growing in frequency convergence increased as a function of the size of convergence, controlling for any potential effects of spectro-temporal features of the flow matrices at the individual sites that might have increased the probability of coincidental frequency convergences. We thus conclude that oscillation-frequency convergences across anterior-posterior sites are driven by synergistic interactions.

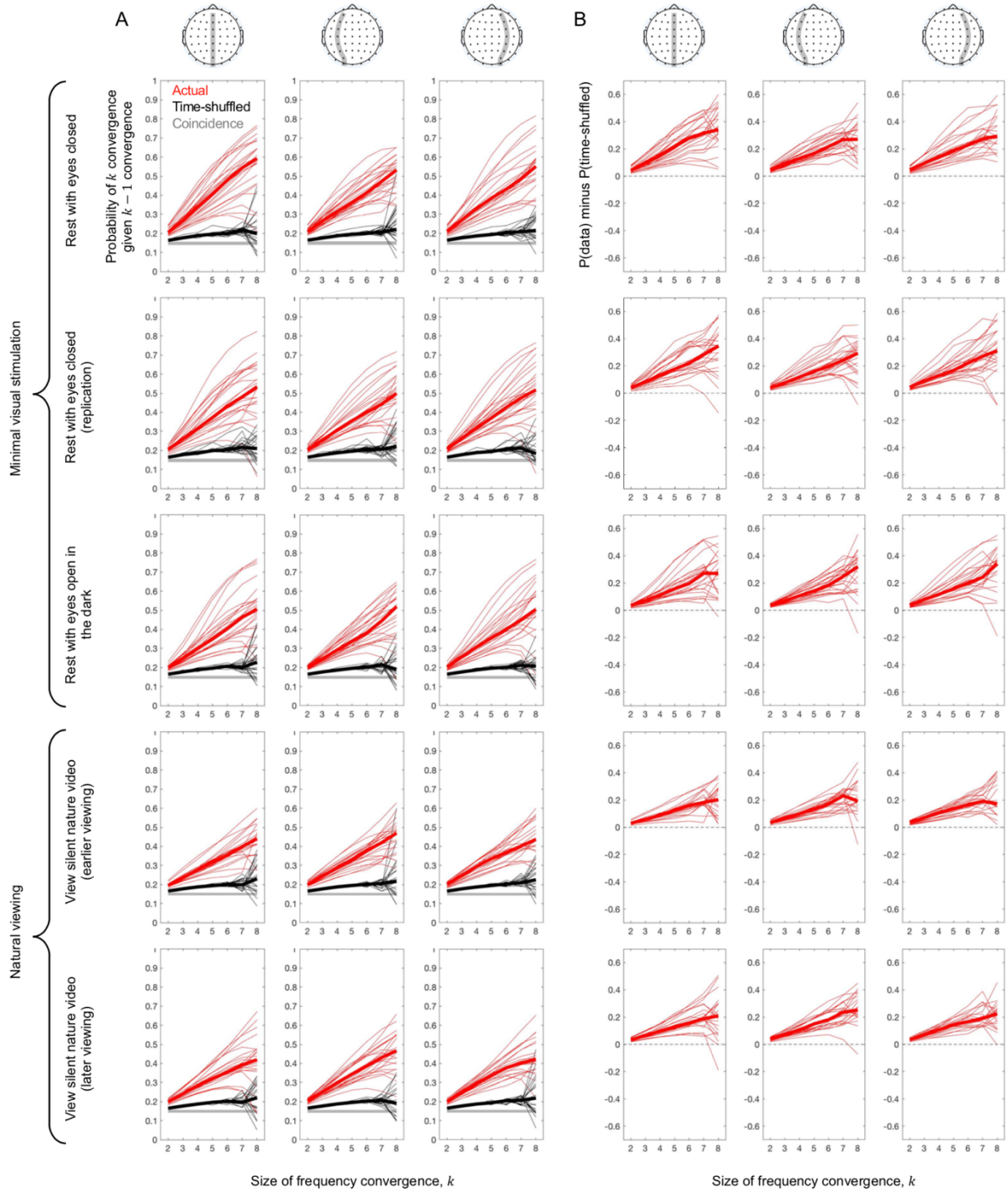

Fig 5. The probability of k convergence (oscillation-frequency convergences across k sites) given k-1 convergence, that is, the probability of growing in convergence from k-1 to k, $P(k|k-1)$, as a function of k for the five behavioral conditions (rows). A. $P(k|k-1)$ for the actual data (red), their time-shuffled controls (black, averaged across 20 versions), and the probabilities expected if oscillation-frequency convergences occurred randomly (gray). **B.** $P(k|k-1)$ for the actual data minus $P(k|k-1)$ for the corresponding time-shuffled controls. Thin lines show individual participants' values while the thick lines show the median values. The data are somewhat noisy for high convergences (for $k = 7$ and especially for $k = 8$) as their instances were relatively rare especially for the time-shuffled controls (see Fig 4). In both parts A and B, the data for the anterior-posterior sites along the midline and those in the left and right hemispheres are shown in the first, second, and third column, respectively. Note that the probability of increasing in frequency convergence generally increased as the number of frequency-converged sites increased, suggesting that oscillation-frequency convergences across anterior-posterior sites are driven by synergistic interactions.

What mechanisms might mediate the synergistic interactions? Oscillatory neural synchronizations occurring in multiple regions at a matched frequency may enhance one another. In turn, the increased oscillatory synchronizations in those frequency-matched regions may facilitate the spreading of oscillatory synchronizations in neighboring regions. In our EEG data, regional oscillatory synchronizations are reflected in the wavelet-extracted oscillatory powers at the identified oscillation frequencies at each site. Thus, if synergistic oscillation-frequency convergences were mediated by convergence-driven inter-regional enhancements of oscillatory synchronizations, larger frequency convergences should be associated with higher oscillatory powers at participating sites.

To evaluate this possibility, we temporally averaged oscillatory powers at each site separately for each size of frequency convergence, k. For instance, we averaged oscillatory powers at AFz when its oscillation frequencies did not converge with any other sites ($k = 1$), when its oscillation frequencies converged with one other site ($k = 2$), when its oscillation frequencies converged with two other sites ($k = 3$), and so on. This yielded the average oscillatory power at each site as a function of the size of frequency convergence in which it participated. However, we may obtain a spurious association between higher power and larger frequency convergence due to general frequency-flow characteristics. For example, if dominant high-power oscillations were concentrated within a narrow frequency range at most sites, those high-power oscillations would coincide with high probability. To account for such confounds due to biased coincidences, we applied the same analysis to the corresponding time-shuffled controls. Any coincidental effects due to general frequency-flow characteristics would be equivalent for the actual data and their time-shuffled controls. Thus, for each site, we computed its average oscillatory power minus the value obtained with the corresponding time-shuffled control (averaged across 20 versions) as a function of the size of frequency convergence in which it participated. To facilitate comparisons of these power-by-convergence functions across sites, behavioral conditions, and participants, we normalized each function (actual minus control) by dividing it by its maximum actual power.

Fig 6 shows the (normalized) average oscillatory power at each site (color coded from dark blue [posterior] to yellow [anterior]) as a function of the size of frequency convergence in which it participated. The open circles indicate Bonferroni-corrected (for eight convergence sizes) significant difference from the control level (i.e., zero) at α=0.05 (two-tailed). In all five behavioral conditions, the oscillatory power generally increased as a function of the size of frequency convergence at all sites (except at the anterior-most site in some cases; see yellow curves in Fig 6), rising significantly above the control levels at convergences of 4-5 sites and

steeply increasing at higher convergences. These increases were somewhat steeper under minimal visual stimulation than in natural viewing (the top three vs. bottom two rows in Fig 6). Overall, the results summarized in Fig 6 are consistent with the aforementioned possibility that the synergistic oscillation-frequency convergences may be mediated by inter-regional enhancements of oscillatory synchronization.

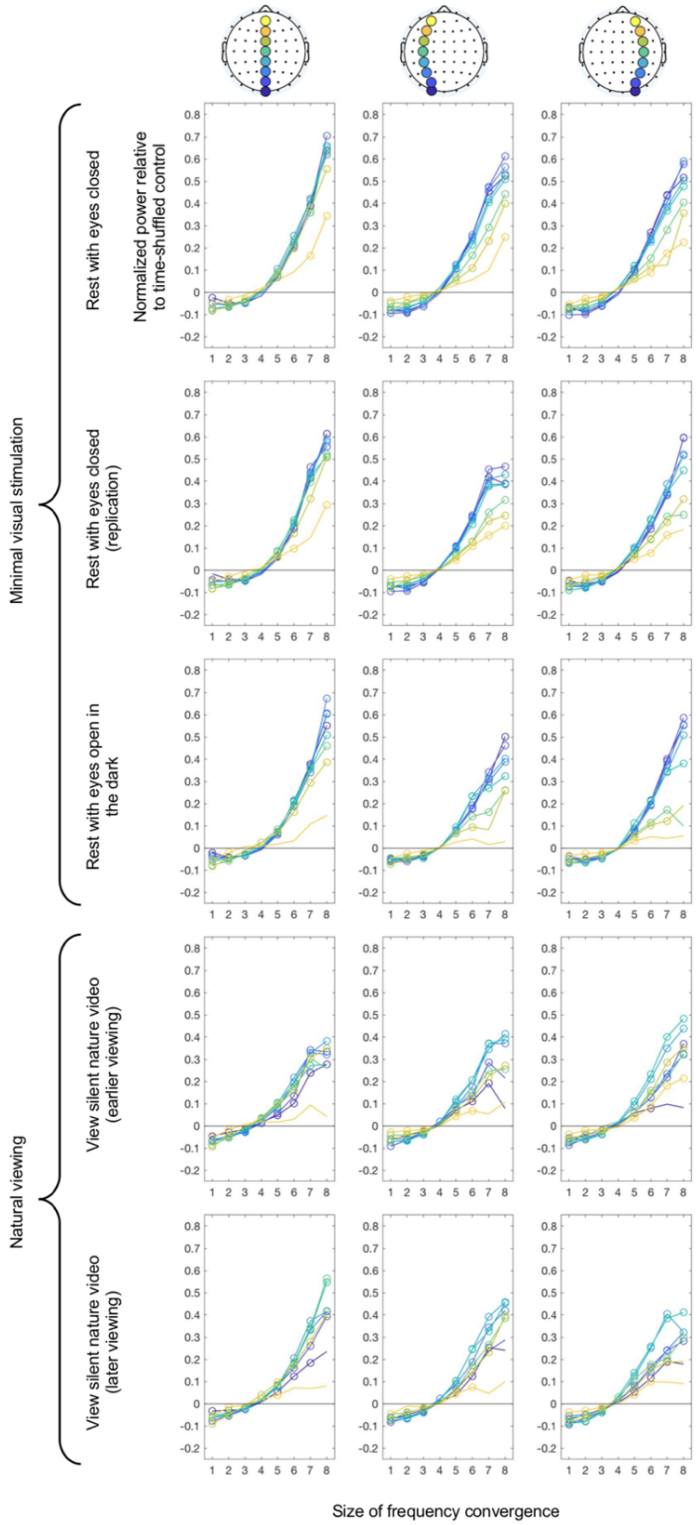

Fig 6. Time-averaged oscillatory power at anterior-posterior sites along the midline (left column) and in the left (middle column) and right (right column) hemispheres (with sites color-coded from dark blue [posterior] to yellow [anterior]), as a function of the size of frequency convergence, for the five behavioral conditions (rows). The power values were computed relative to those obtained with the corresponding time-shuffled controls (averaged across 20 versions) and normalized to the maximum actual power for each function (per site per behavioral condition per participant). The average values across participants are plotted, with each open circle indicating Bonferroni-corrected (for eight convergence sizes) statistical significance (α=0.05, two-tailed) relative to zero (control levels). Most sites in all behavioral conditions showed accelerated increases in power when they participated in frequency convergences of four or more sites.

To gain some insights into how anterior-posterior frequency convergences spread, we examined each site's propensities for joining frequency convergences of different sizes. For example, in a simple case where frequency convergences always spread sequentially from site S1 to S8, frequency convergences of two sites would predominantly involve S1 and S2, convergences of three sites would predominantly involve S1, S2, and S3, convergences of four sites would predominantly involve S1, S2, S3, and S4, and so on. Propensities for each site to be included in frequency convergences of different sizes k were computed as the ratio of the actual instances to those obtained with the corresponding time-shuffled controls (averaged across 20 time-shuffles). For example, a value of 0.8 would indicate that the number of instances of a particular site being involved in frequency convergences of size k was 80% relative to the corresponding control level, and a value of 3.5 would indicate that the number of instances was 3.5 times as frequent as the corresponding control level, with 1 indicating the levels expected from coincidences given the spectro-temporal features of the flow matrices at the individual sites.

Anterior-posterior oscillation-frequency convergences appear to spread differently along the midline than in the left and right hemispheres. Along the midline, the instances of participating in frequency convergences of 3-7 sites were consistently reduced for the posterior-most and anterior-most sites; note that the instances of participating in frequency convergences of all 8 sites were necessarily equal for all sites. The flattened inverted-U pattern was consistently observed in all behavioral conditions (black curves in Fig 7A) and for most participants (gray curves in Fig 7A). For frequency convergences of 2 sites and singletons, we obtained the pattern that was opposite to those in Fig 7A (not shown), indicating that the posterior-most and anterior-most sites had elevated tendencies to generate isolated oscillations that did not spread beyond a pair of sites. Overall, these results suggest that frequency convergences along the midline can develop from most sites except that the posterior-most and anterior-most sites tend to join later.

In the left and right hemispheres, the instances of participating in frequency convergences of 3-7 sites were progressively diminished from posterior to anterior sites, with the negative monotonicity (measured as Spearman's r) being statistically significant in most cases across all behavioral conditions (Fig 7B and 7C). It appears that the negative monotonicity was generally stronger under minimal visual stimulation than in natural viewing. As above, these patterns reversed for frequency convergences of 2 sites and singletons (not shown), indicating that the sites that participated less in larger frequency convergences had elevated tendencies to generate isolated oscillations that did not spread beyond a pair of sites. Overall, these results

suggest that in the left and right hemispheres frequency convergences tend to spread from posterior to anterior sites.

Note that the instances of participating in frequency convergences of 3 sites were below the control levels in all cases (Fig 7A, 7B, and 7C), suggesting that synergistic frequency convergences operate on a threshold of more than 3 converged sites. This is consistent with the results above that oscillatory powers were consistently below the control levels for frequency convergences of 3 or less sites (Fig 6).

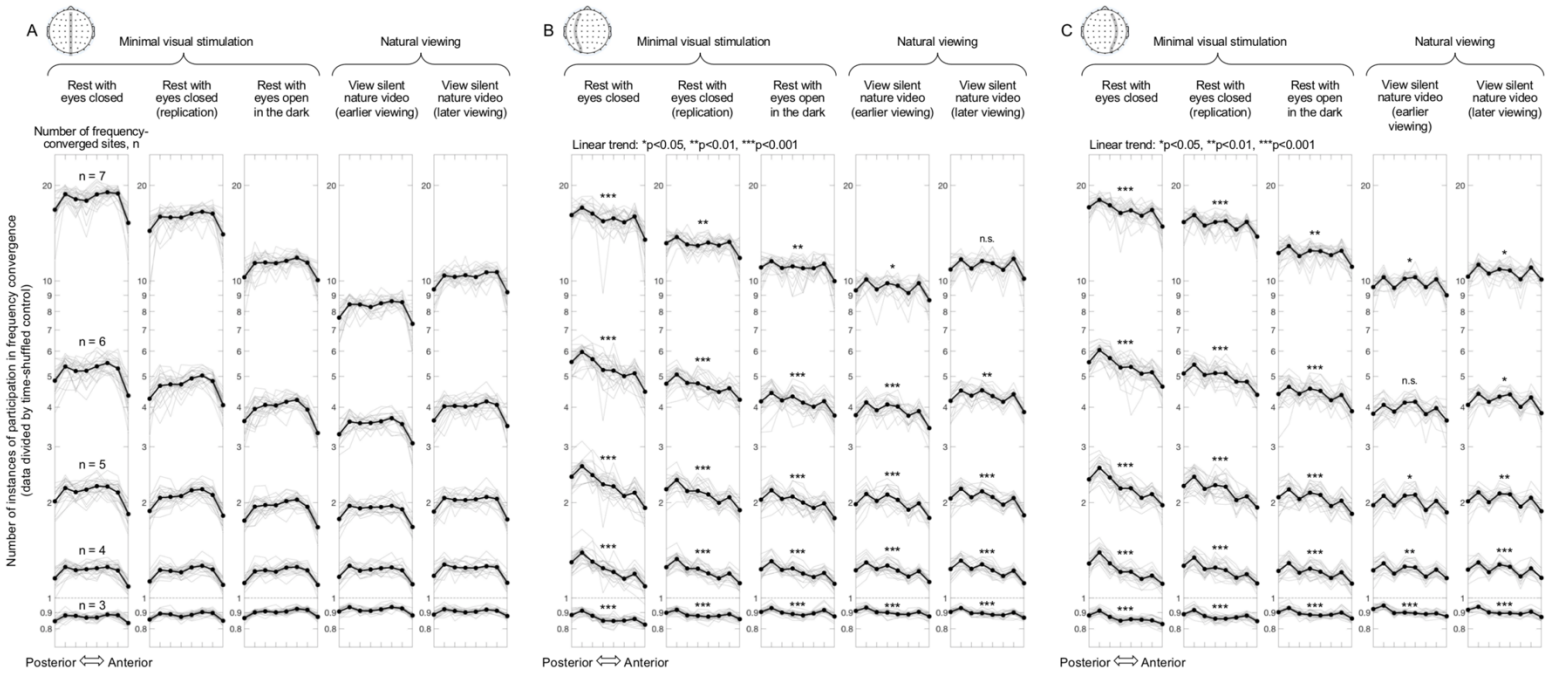

Fig 7. The number of instances of each site along the anterior-posterior axis participating in frequency convergences of 3-7 sites, along the midline (A) and in the left (B) and right (C) hemispheres, in the five behavioral conditions (columns). The values were divided by the corresponding values obtained with the time-shuffled controls (averaged across 20 versions). For example, a value of 0.8 indicates that the actual instances were 80% of the control instances, a value of 3.5 indicates that the actual instances were 3.5 times as frequent as the control instances, and so on. The solid curves show the geometric means while the gray curves show the values from individual participants aligned at the corresponding geometric means. Along the midline (**A**), the posterior-most and anterior-most sites were less likely to be included in frequency convergences of 3 or more sites, whereas in the left (**B**) and right (**C**) hemispheres, further anterior sites were progressively less likely to be included in frequency convergences of 3 or more sites, yielding significant negative slopes. The patterns for frequency convergences of 2 and singletons (not shown) were opposite to those shown, confirming that the sites that were less involved in larger frequency convergences had elevated tendencies to generate isolated oscillations that did not spread beyond a pair of sites.

Given that anterior-posterior oscillation-frequency convergences appear to be synergistically driven, what functions might they serve? Investigating this question would require explorations of behavioral tasks whose performances may be influenced by intrinsic oscillation-frequency convergences. Here we indirectly investigated the potential functions of oscillation-frequency convergences by examining the phase relations induced by frequency convergences. For example, if frequency convergences induced a phase gradient with progressive phase lags from anterior to posterior sites, one could infer that frequency convergences facilitate a flow of information from anterior to posterior regions.

We computed sequential phase differences from posterior to anterior. For example, for the anterior-posterior axis along the midline, we computed the phase of POz minus the phase of Oz, the phase of Pz minus the phase of POz, the phase of CPz minus the phase of Pz, the phase of Cz minus the phase of CPz, the phase of FCz minus the phase of Cz, the phase of Fz minus the phase of FCz, and the phase of AFz minus the phase of Fz. These sequential phase differences were computed wherever the size of frequency convergence was two or larger in the flow-convergence matrices (e.g., Fig 3), and were averaged (as complex angles) across all instances but separately for each size of frequency convergence. Because of the temporal averaging, this analysis detected phase gradients only if they were consistent across all occurrences of frequency convergences of each size over ~5 min.

To visualize the phase gradients, we spatially integrated the sequential pairwise phase differences from the posterior to anterior sites while arbitrarily setting the phase at the posterior-most site to zero (i.e., we cumulatively summed the sequential pairwise phase differences from posterior to anterior). A negative phase gradient (a negative slope) indicates that anterior sites increasingly lagged in phase, suggestive of a flow of information in the anterior direction, whereas a positive phase gradient (a positive slope) indicates that posterior sites increasingly lagged in phase, suggestive of a flow of information in the posterior direction.

Upon examination of the phase gradients obtained from each participant, we noted that they classified into two prototypes. Clear examples of those are shown in Fig 8B in the top panel. One prototype consisted of generally negative phase gradients from posterior to anterior, whereas the other prototype consisted of generally positive phase gradients from posterior to anterior. Both gradients became steeper as the size of frequency convergence increased.

To determine how consistently the phase-gradient patterns from individual participants classified into these prototypes, we examined the distribution of phase-gradient patterns in the two-dimensional space defined by (1) the overall average phase and (2) the correlation between the average phase and the size of frequency convergence. In the negative-gradient prototype,

the overall average phase was negative and the average phase of each phase curve was negatively correlated with the size of frequency convergence (more negative with larger frequency convergence). In the positive-gradient prototype, the overall average phase was positive and the average phase of each phase curve was positively correlated with the size of frequency convergence (more positive with larger frequency convergence). Thus, in the two-dimensional space defined by the overall average phase on the x-axis and the average-phase-vs-convergence-size correlation on the y-axis with the lines x=0 and y=0 dividing the space into four quadrants, the negative-gradient prototype (negative overall average phase and negative average-phase-vs-convergence-size correlation) is represented in the lower-left quadrant while the positive-gradient prototype (positive overall average phase and positive average-phase-vs-convergence-size correlation) is represented in the upper-right quadrant. We excluded from this analysis the phase curves for the largest convergence (i.e., convergence of all sites) which tended to be noisy due to the relatively rare occurrences of the maximal convergence (Fig 4).

As shown in Fig 8A and 9A, most participants populated either the lower-left quadrant, generating phase-gradient patterns similar to the negative-gradient prototype (see Fig 8B and 9B corresponding to the red rectangles), or the upper-right quadrant, generating phase-gradient patterns similar to the positive-gradient prototype (see Fig 8B and 9B corresponding to the blue rectangles).

Interestingly, under minimal visual stimulation (especially with eyes closed), the negative- and positive-gradient patterns spatially segregated, with the negative gradients dominating along the midline (first panels in Fig 8A) whereas the positive gradients dominating in the left (second panels in Fig 8A) and right hemispheres (third panels in Fig 8A). To confirm this spatial segregation, we computed the correlations between the average phase gradient patterns (averaged across frequency-convergence sizes per participant) between each pair of anterior-posterior axes (left hemisphere vs. right hemisphere, left-hemisphere vs. midline, and right-hemisphere vs. midline). Indeed, the left- and right-hemisphere gradients were generally positively correlated whereas they were both negatively correlated with the midline gradient in the minimal-visual-stimulation conditions (Fig 8C, especially in the top and middle panels for the eyes-closed conditions). This spatial segregation dissipated in the natural viewing conditions. The participants in those conditions relatively evenly populated the lower-left (indicative of the negative-gradient prototype) and the upper-right (indicative of the positive-gradient prototype) quadrants for each of the three anterior-posterior axes, along the midline (first panels in Fig 9A) and in the left (second panels in Fig 9A) and right (third panels in Fig 9A) hemispheres, with no significant correlations of gradient patterns between any pair of anterior-posterior axes (Fig 9C).

Fig 8. Two general types of posterior-to-anterior phase gradients observed during inter-site convergences of oscillation frequencies. The three large panels show data from the three behavioral conditions under minimal visual stimulation, rest with eyes closed, its replication, and rest with eyes open in the dark. A. Two-dimensional space defined by the overall average phase (averaged across anterior-posterior sites and frequency-convergence sizes) on the x-axis and the correlation between the average phase (computed per frequency-convergence size) and the size of frequency convergence (Spearmen's r) on the y-axis, shown separately for the three anterior-posterior axes, along the midline (first panel) and in the left (second panel) and right (third panel) hemispheres. The x=0 and y=0 lines divide the space into four quadrants. Each circle indicates a participant. Note that most participants populated the lower-left quadrant for the anterior-posterior sites along the midline (red rectangle in first columns) whereas they populated the upper-right quadrant for the anterior-posterior sites in the left- and right-hemispheres (blue rectangles in second and third columns). **B.** Phase gradients (averaged across relevant participants) for each quadrant in A that included five or more participants. Note that the lower-left quadrant is characterized by generally negative posterior-to-anterior phase gradients that became steeper (more negative) as the size of frequency convergence increased. In contrast, the upper-right quadrant is characterized by generally positive posterior-to-anterior phase gradients that became steeper (more positive) as the size of frequency convergence increased. **C.** Correlations (Fisher Z transformed Pearson's r) between the average phase-gradient patterns (averaged across frequency-convergence sizes per participant) between each pair of anterior-posterior axes (left hemisphere vs. right hemisphere, left hemisphere vs. midline, and right hemisphere vs. midline). Consistent with the fact that most participants showed negative phase gradients along the midline and positive phase gradients in the left and right hemispheres, we generally obtained positive correlations between the left and right hemispheres but negative correlations between those and the midline. The black bars show the means and the gray lines show data from individual participants.

Fig 9. Two general types of posterior-to-anterior phase gradients observed during inter-site convergences of oscillation frequencies. The formatting of this figure is the same as Fig 8, but it shows data from the two natural viewing conditions, the earlier and later viewings of a silent nature video. Again, most participants populated either the lower-left quadrant (red rectangles) characterized by generally negative posterior-to-anterior phase gradients that became steeper (more negative) as the size of frequency convergence increased, or the top-right quadrant (blue rectangles) characterized by generally positive posterior-to-anterior phase gradients that became steeper (more positive) as the size of frequency convergence increased (**A** and **B**). However, unlike under minimal visual stimulation (Fig 8), participants were relatively evenly distributed between the lower-left and upper-right quadrants for each of the three anterior-posterior axes (**A**) with no consistent pairwise correlations between the average phase-gradient patterns between any of the three anterior-posterior axes (**C**).

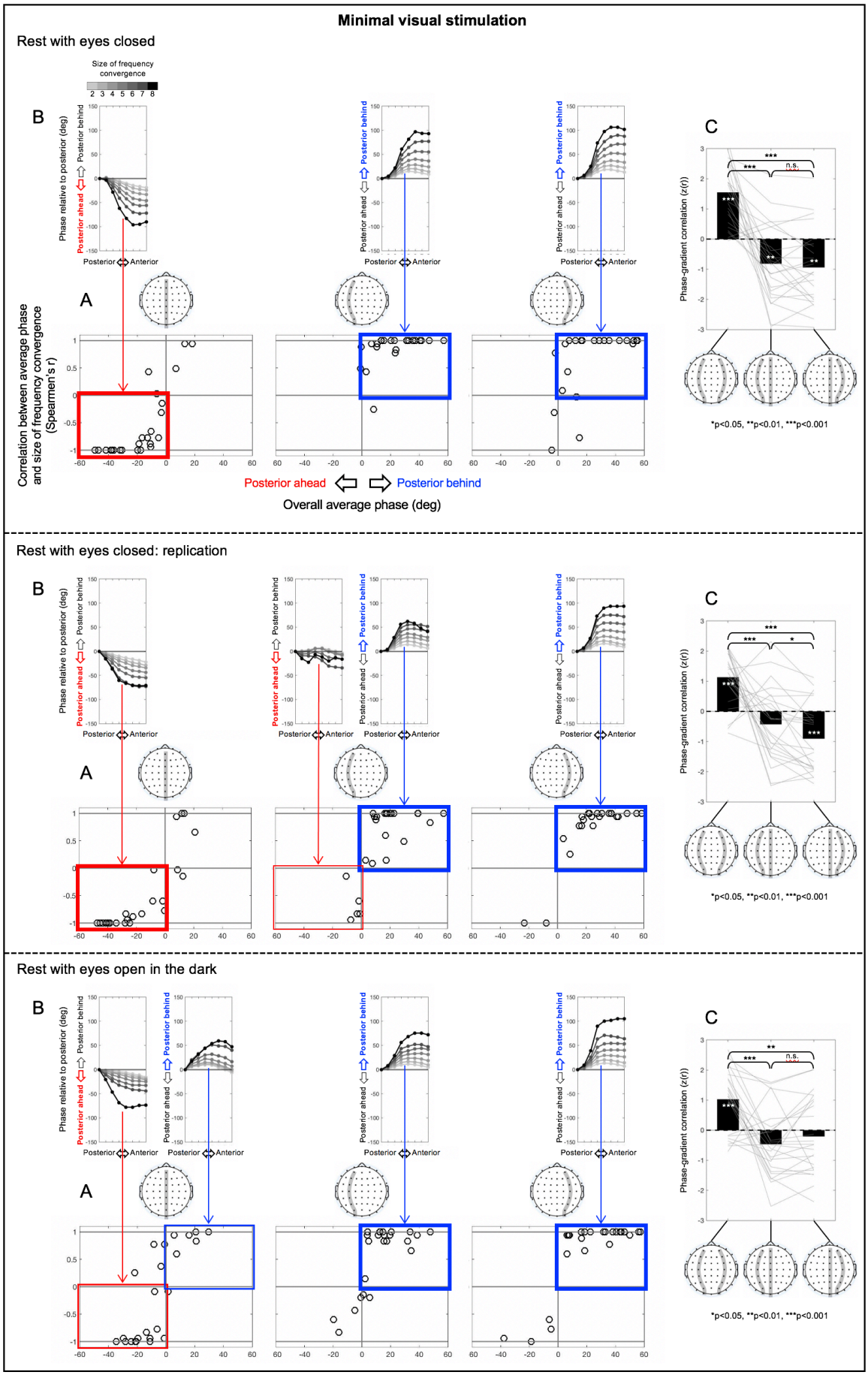
Minimal visual stimulation
Rest with eyes closed
Size of frequency convergence
2 3 4 5 6 7 8
B
A
C
Phase relative to posterior (deg)
Posterior behind
Posterior ahead
Posterior
Anterior
Correlation between average phase and size of frequency convergence (Spearmen's r)
Phase-gradient correlation (z(r))
***
n.s.
**
*p<0.05, **p<0.01, ***p<0.001
Posterior ahead
Posterior behind
Overall average phase (deg)
Rest with eyes closed: replication
*
Rest with eyes open in the dark

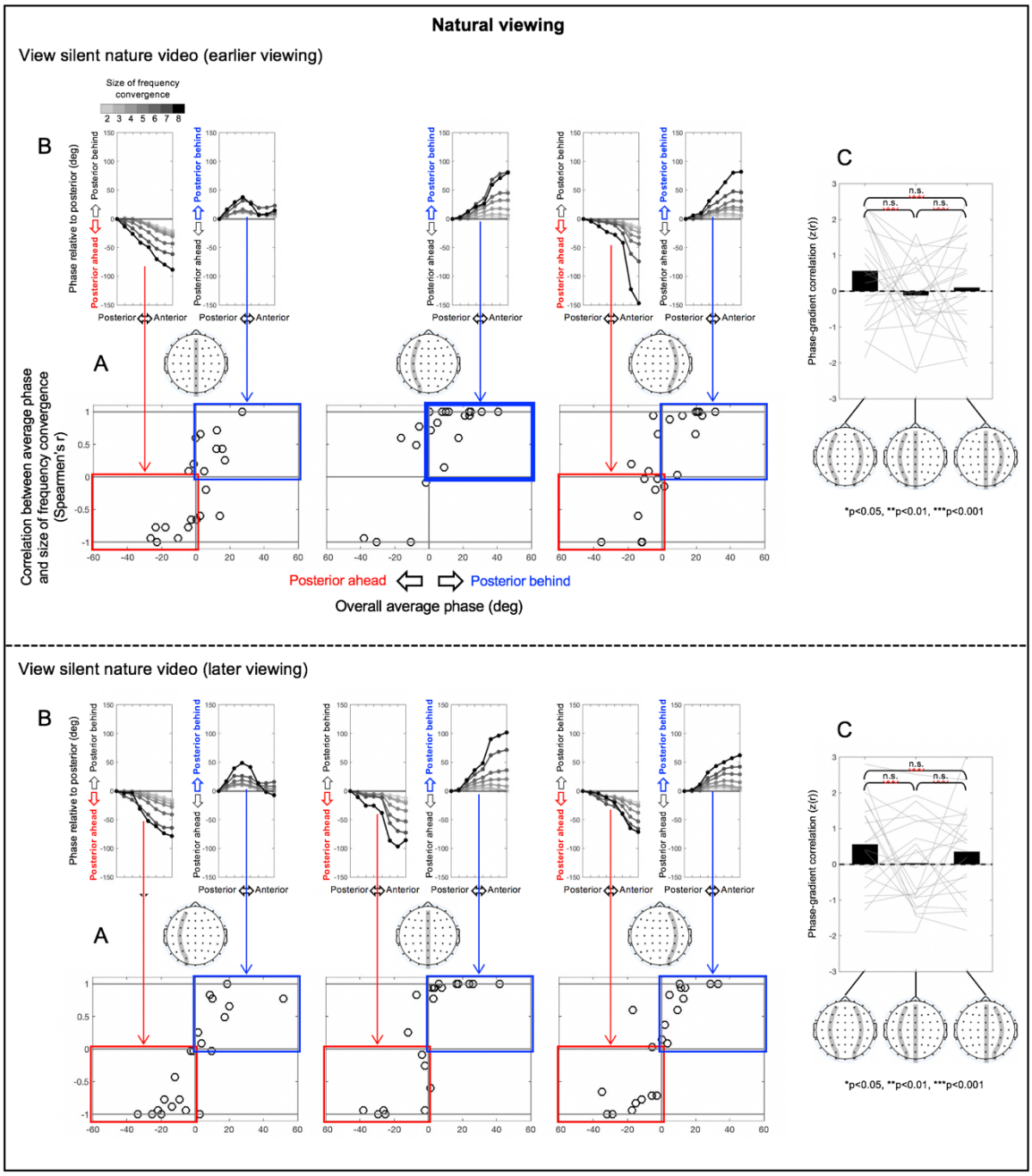

These phase-gradient patterns remained relatively stable over time, yielding phase-clustering values (the modulus of time-averaged complex phase differences ranging between 0 and 1) of ~0.7 above chance levels (computed with the assumption of random sampling from a uniform angular distribution, well described by a power function of the number of instances). The stability of sequential pairwise phase differences was relatively constant along the midline (left column in Fig 10A), but it varied in the left and right hemispheres (left column in Fig 10B and 10C). The patterns of these variations were generally unaffected by the size of frequency convergence (right column in Fig 10A, 10B, and 10C). Further, the overall stability of phase relations was not systematically affected by the size of frequency convergence along the midline

(right column in Fig 10A), though the stability was somewhat reduced by larger frequency convergences in the left and right hemispheres especially in the natural viewing conditions (right column in Fig 10A and 10B, especially in the bottom two rows). Overall, oscillation-frequency convergences did not have substantial effects on the stability of phase relations.

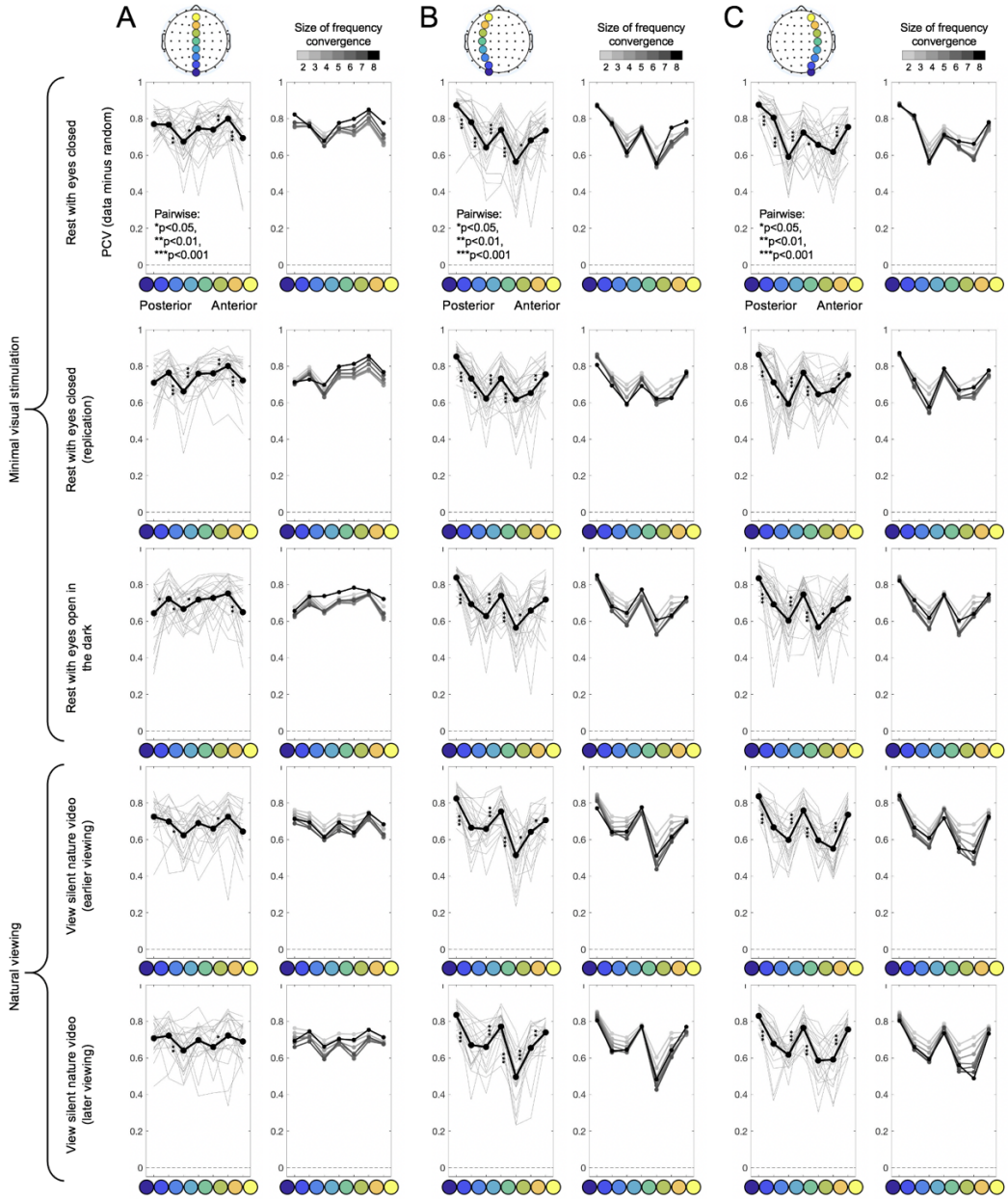

Fig 10. Phase-clustering values (PCV's, also known as phase-locking values or PLV's) for sequential pairs of anterior-posterior sites (cooler to warmer colors) along the midline (A) and in the left (B) and right (C) hemispheres for the five behavioral conditions (rows). Left panels. Average PCV's (black curves) and those for individual participants (gray curves). Asterisks indicate different levels of statistical significance for comparisons between successive pairs of values. **Right panels.** Average PCV's shown separately for frequency-convergences of 2 through 8 sites (lighter to darker colors). PCV's for random angular distributions of the corresponding numbers of instances have been subtracted so that the value of zero (dashed lines) indicates chance levels.

While we conducted our oscillation-frequency convergence analyses in the extended alpha range (5-15 Hz), the question remains whether large frequency convergences occurred evenly in this range or in a specific subrange(s)? We thus computed average frequency-convergence size as a function of frequency by taking each participant's wavelet-frequency-(row)-by-time-(column) flow-convergence matrix (per anterior-posterior axis per condition) and averaged the convergence sizes (omitting zeros where no oscillations occurred at any sites) across time for each wavelet frequency. To control for any influences of spectro-temporal characteristics at individual sites (see above), we subtracted the values obtained from the corresponding time-shuffled controls (averaged across 20 versions). To avoid the analysis being unduly influenced by participants who yielded large convergence sizes, we normalized each participant's average-convergence-size-by-frequency curve by dividing each value by the average value across all frequencies (per anterior-posterior axis per condition). As shown in Fig 11, the size of oscillation-frequency convergence was substantially elevated in the conventional alpha range (8-13 Hz) for all anterior-posterior axes in all conditions. Thus, the results reported here primarily reflect oscillation-frequency convergences occurring in the alpha range.

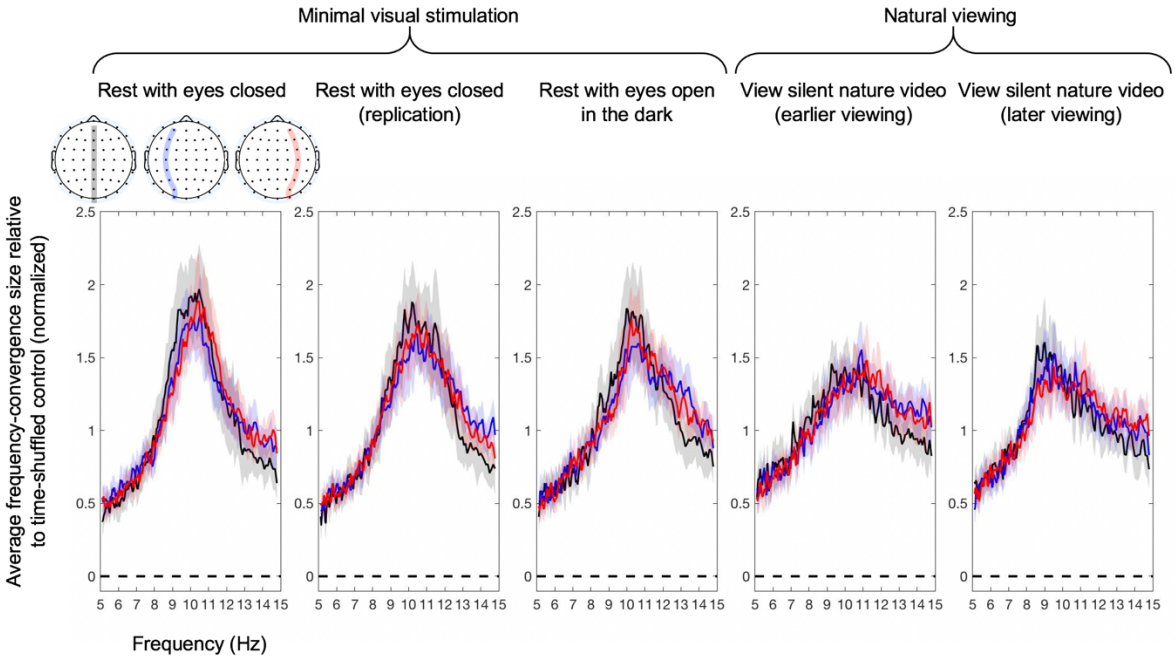

Fig 11. Time-averaged frequency-convergence size as a function of wavelet frequency (Hz) for the anterior-posterior axes along the midline (black) and in the left (blue) and right (red) hemispheres for the five behavioral conditions. The values are relative to those obtained with the corresponding time-shuffled controls (averaged across 20 versions). The curve from each participant was normalized by dividing each value by the average value across all frequencies. Note that oscillation-frequency convergences were substantially elevated in the conventional alpha range (8-13 Hz) in all cases. The shaded areas represent the 95% confidence intervals (computed with participants as the random effect).

Discussion

We examined the dynamics of spontaneous anterior-posterior oscillation-frequency convergences in an extended alpha range (5-15 Hz), along the midline and in the left and right hemispheres, under minimal visual stimulation (resting with eyes closed or open in the dark) and in natural viewing (watching a silent nature video). The instances of large frequency convergences (involving four or more sites out of eight) were elevated for all participants in all behavioral conditions relative to the time-shuffled controls, suggesting that oscillation frequencies dynamically converge across anterior-posterior sites over and above any tendencies for dominant oscillations in relatively narrow frequency bands to randomly coincide. The probability of an additional site joining a frequency convergence increased as more sites frequency-converged, suggesting that oscillation-frequency convergences are driven by synergistic interactions. The oscillatory power at participating sites increased as more sites frequency-converged (especially as five of more sites converged), suggesting that oscillation-frequency convergences are driven by synergistic interactions wherein regional synchronizations boosted by inter-regional frequency matching facilitate the entrainment of additional regions. This interpretation is consistent with previous reports of elevated oscillatory power in brain regions engaged in strong and/or extensive phase locking with other regions [e.g., 58-59].

Given our results suggest that spontaneous anterior-posterior oscillation-frequency convergences are driven by synergistic interactions, what functions might they serve? Although we did not include behavioral experiments to compare frequency convergences with behavioral task performances, some inferences can be made from the two anterior-posterior phase gradients that we observed during oscillation-frequency convergences. One was a negative gradient from posterior to central sites (plateauing from central to anterior sites)—the posterior-ahead gradient. The other was a positive gradient from posterior to central sites (plateauing from central to anterior sites)—the posterior-behind gradient. These gradients remained relatively stable over a five-minute period, yielding the average PCV's of ~0.7 above chance levels.

The posterior-ahead gradient is consistent with the interpretation (though it does not necessarily imply) that information flows out of posterior cortex in the sense that oscillations ahead in phase may be causing those behind in phase. Similarly, the posterior-behind gradient is consistent with the interpretation that information flows to posterior cortex. These gradients generally became steeper as the size of frequency convergence increased. A steeper phase

gradient suggests stronger directionality of information flow provided that the stability of the phase gradient was not reduced by the increased slope. The stability (in PCV's relative to chance levels) was not systematically affected by the size of frequency convergence along the midline, though it somewhat reduced with larger frequency convergences in the left and right hemispheres especially in natural viewing. Thus, the steeper slopes associated with larger frequency convergences suggest stronger directionality of phase gradients at least along the midline as well as in both hemispheres under minimal visual stimulation. In other words, frequency convergences enhance the directionality of information flows to and from posterior cortex especially along the midline, but potentially also in both hemispheres especially under minimal visual stimulation.

The anterior-posterior phase gradients we observed were based on phase relations that remained stable (averaged) over relatively long (5 minute) periods. Further, those phase gradients were piece-wise consistent whether only a few sites or most sites frequency-converged except that the gradients became steeper when more sites frequency-converged. As such, the posterior-behind and posterior-ahead gradients observed here do not imply macroscopic traveling waves, which have been shown to generally propagate from posterior to anterior when eyes are open and from anterior to posterior when eyes are closed [e.g.,30,60-61]. Further, one of the primary mechanisms of traveling waves is a linear spatial gradient of oscillation frequencies, wherein a wave travels from higher-frequency regions to lower-frequency regions [e.g., 62]. In contrast, the stable anterior-posterior phase gradients we observed occurred when participating regions oscillated at matched frequencies. Thus, macroscopic traveling waves of various amplitudes likely occur in either direction in different moments against the background of the stable phase gradients we observed that are enhanced by larger oscillation-frequency convergences.

How did anterior-posterior oscillation-frequency convergences depend on the midline versus within-hemisphere axes and behavioral conditions? The prevalence of oscillation-frequency convergences, the increased probability of growing in convergence with increased size of frequency convergence, and the increased oscillatory power with increased size of frequency convergence, were relatively independent of the location of the anterior-posterior axis and behavioral conditions (except that they all somewhat diminished in natural viewing relative to under minimal visual stimulation). This suggests that the synergistic interactions that likely drive spontaneous oscillation-frequency convergences are ubiquitous. In contrast, the manner of spreading of frequency convergences and the occurrences of the posterior-behind and

posterior-ahead phase gradients depended on the location of the anterior-posterior axis and behavioral conditions.

Frequency convergences spread differently along the midline versus within each hemisphere. Along the midline, the anterior-most and posterior-most sites joined oscillation-frequency convergences with lower likelihood, with the pattern consistent across all behavioral conditions. This suggests that anterior-posterior frequency convergences along the midline tend to spread from any site except the anterior-most and posterior-most sites. In the left and right hemispheres, more anterior sites joined oscillation-frequency convergences with progressively lower likelihoods. This trend was stronger under minimal visual stimulation than in natural viewing. This suggests that anterior-posterior frequency convergences within each hemisphere tend to spread from posterior to anterior regions especially under minimal visual stimulation.

The posterior-ahead and posterior-behind phase gradients were spatially segregated under minimal visual stimulation. When participants rested with their eyes closed, the posterior-ahead gradients predominantly occurred along the midline whereas the posterior-behind gradients predominantly occurred within the left and right hemispheres. This spatial segregation was unique to resting with eyes closed as the segregation became less clear when participants rested with their eyes open in a dark room and disappeared when they viewed a silent nature video. This suggests that most people, when they close their eyes, default to the pattern of information flow where the information carried primarily in the alpha range (8-13 Hz) flows to posterior cortex within each hemisphere and flows out of posterior cortex along the midline. Future research may investigate how closing eyes induces these spatially structured anterior-posterior information flows and how they may influence mentation.

In summary, previous work typically examined inter-regional phase coherence in specific frequency bands (without identifying oscillation frequencies) to study frequency-specific functional networks. We took a complementary approach of tracking variations in regional oscillation frequencies to study how brain regions spontaneously converged their oscillation frequencies to stably interact with one another via oscillatory phase locking. Given the known functional relevance of anterior-posterior neural interactions, the presence of various neuroanatomical and neurophysiological feature gradients along the anterior-posterior axis, and the relevance of theta, alpha, and low-beta bands in organizing gamma activity as well as mediating perceptual, attentional, and memory processes (see the introduction section), we examined inter-regional oscillation-frequency convergences along the anterior-posterior axis in an extended alpha range (5-15 Hz). Our results primarily reflected oscillation-frequency convergences within the conventional alpha range (8-13 Hz) where frequency convergences

predominantly occurred. With regard to their potential mechanism, our results suggest that inter-regional oscillation-frequency convergences are driven by synergistic interactions wherein regional synchronizations boosted by inter-regional frequency matching facilitate the entrainment of additional regions. With regard to their potential function, our results suggest that inter-regional oscillation-frequency convergences generate stable posterior-behind gradients—potentially facilitating information flows to posterior cortex—and posterior-ahead phase gradients—potentially facilitating information flows out of posterior cortex, which increase in directionality as more sites frequency-converge and spatially segregate when eyes are closed. Future research may investigate the behavioral relevance of these characteristics of anterior-posterior oscillation-frequency convergences by relating them to task performances.

References

[1] Buzsaki, G. (2006). *Rhythms of the Brain*, Oxford University Press.

[2] Fries, P. (2005). A mechanism for cognitive dynamics: neural communication through neural coherence. *Trends in Cognitive Sciences, 9(10)*, 474-480.

[3] Fries, P. (2015). Rhythms for cognition: Communication through coherence. *Neuron, 88*, 220-235.

[4] Palva, J. M., Palva, S., & Kaila, K. (2005). Phase synchrony among neuronal oscillations in the human cortex. *Journal of Neuroscience, 25(15)*, 3962-3972.

[5] Palva, S., & Palva, J. M. (2012). Discovering oscillatory interaction networks with M/EEG: challenges and breakthroughs. *Trends in Cognitive Sciences, 16(4)*, 219-230.

[6] Lobier, M, Palva, J. M, & Palva, S. (2018). High-alpha band synchronization across frontal, parietal and visual cortex mediates behavioral and neuronal effects of visuospatial attention. *NeuroImage, 165*, 222-237.

[7] Marzetti, L., Basti, A., Chella, F., D'Andrea, A., Syrjälä, J, & Pizzella, V. (2019). Brain functional connectivity through phase coupling of neuronal oscillations: A perspective from magnetoencephalography. *Frontiers in Neuroscience, 13*: https://doi.org/10.3389/fnins.2019.00964

[8] Keitel, A. & Gross, J. (2016). Individual human brain areas can be identified from their characteristic spectral activation Fingerprints. *PLoS Biology, 14(6)*: e1002498. doi:10.1371/journal. pbio.1002498

[9] Mahjoory, K., Schoffelen, J.-M., Keitel, A., & Gross, J. (2020). The frequency gradient of human resting-state brain oscillations follows cortical hierarchies. *eLife 9*: e53715. DOI: https://doi.org/10.7554/eLife.53715

[10] Mierau, A., Klimesch, W., & Lefebvre, J. (2017). State-dependent alpha peak frequency shifts: experimental evidence, potential mechanisms, and functional implications. Neuroscience, 360, 146-154.

[11] Benwell, C.S. Y., London, R. E., Tagliabue, C. F., Veniero, D., Gross, J., Keitel, C., & Thut, G. (2019). Frequency and power of human alpha oscillations drift systematically with time-on-task. *NeuroImage, 192*, 101-114.

[12] Amor, F., Rudrauf, D., Navarro, V., N'diaye, K., Garnero, L., Martinerie, J., & Le Van Quyen, M. (2005). Imaging brain synchrony at high spatio-temporal resolution: application to MEG signals during absence seizures. *Signal Processing, 85*, 2101-2111.

[13] Rudrauf, D., Douiri, A., Kovach, C., Lachaux, J.-P., Cosmelli, D., Chavez, M., Adam, C., Renault, B., Martinerie, J., & Le Van Quyen, M. (2006). Frequency flows and the time-frequency dynamics of multivariate phase synchronization in brain signals. *NeuroImage, 31*, 209-227.

[14] Mallat, S. (2009). A Wavelet Tour of Signal Processing: The Sparse Way. Academic Press.

[15] de Pasquale, F., Penna, S. D., Snyder, A. Z., Marzetti, L., Pizzella, V., Romani, G. L., & Corbetta, M. (2012). A cortical core for dynamic integration of functional networks in the resting human brain. *Neuron, 74*, 753-764.

[16] Gonzalez-Castillo, J., & Bandettini, P. A. (2018). Task-based dynamic functional connectivity: recent findings and open questions. *NeuroImage, 180*, 526-533.

[17] Reinhart, R. M. G, & Nguyen, J. A. (2019). Working memory revived in older adults by synchronizing rhythmic brain circuits. *Nature Neuroscience, 22*, 820-827.

[18] Mashour, G. A., Roelfsema, P., Changeux, J.-P., & Dahaene, S. (2020). Conscious processing and the global neuronal workspace hypothesis. *Neuron, 105*, 776-798.

[19] Huntenburg, J. M., Bazin, P. L., & Margulies, D. S. (2018). Large-Scale gradients in human cortical organization. *Trends in Cognitive Sciences 22*, 21–31. DOI: https://doi.org/10.1016/j.tics.2017.11.002, PMID: 29203085

[20] Burt, J. B., Demirtas, M., Eckner, W. J., Navejar, N. M., Ji, J. L., Martin, W.J., Bernacchia, A., Anticevic, A., Murray, J. D. (2018). Hierarchy of transcriptomic specialization across human cortex captured by structural neuroimaging topography. *Nature Neuroscience 21*, 1251–1259. DOI: https://doi.org/10.1038/s41593-018-0195-0, PMID: 300 82915

[21] Palva, S., & Palva, M. (2007). New vistas for α-frequency band oscillations. *Trends in Neurosciences, 30(4)*, 150-158.

[22] Mathewson, K. E., Gratton, G., Fabiani, M., Beck, D. M., & Ro, T. (2010). To see or not to see: prestimulus alpha phase predicts visual awareness. *Journal of Neuroscience, 29*, 2725-2732.

[23] Busch, N. A., & VanRullen, R. (2010). Spontaneous EEG oscillations reveal periodic sampling of visual attention. *Proceedings of the National Academy of Sciences, 107(37)*, 16048-16053.

[24] Klimesch, W. (2012). Alpha-band oscillations, attention, and controlled access to stored information. *Trends in Cognitive Sciences, 16(12)*, 606-617.

[25] Bonnefond, M, & Jensen, O. (2015). Gamma activity coupled to alpha phase as a mechanism for top-down controlled gating. *PLoS ONE, 10(6)*: e0128667, 1-11.

[26] Harris, A. M., Dux, P. E., & Mattingley, J. B. (2018). Detecting unattended stimuli depends on the phase of prestimulus neural oscillations. *Journal of Neuroscience, 38*, 3092–3101.

[27] Bahramisharif, A., van Gerven, M. A. J., Aarnoutse, E., Mercier, M. R., Schwartz, T. H., Foxe, J. J., Ramsey, N. F., & Jensen, O. (2013). Propagating neocortical gamma bursts are coordinated by traveling alpha waves. *Journal of Neuroscience, 33(48)*, 18849-18854. DOI: 10.1523/JNEUROSCI.2455-13.2013

[28] Esghaei, M., Treue, S., & Vidyasagar, T. R. (2022). Dynamic coupling of oscillatory neural activity and its roles in visual attention. Trends in Neurosciences, 45(4), 323-335. DOI: https://doi.org/10.1016/j.tins.2022.01.003

[29] Jensen, O., Gips, B., Bergmann, T. O., & Bonnefond, M. (2014). Temporal coding organized by coupled alpha and gamma oscillations prioritize visual processing. *Trends in Neurosciences, 37(7)*, 357-369.

[30] Zhang, H., Watrous, A. J., Patel, A., & Jacobs, J. (2018). Theta and alpha oscillations are traveling waves in the human neocortex. *Neuron, 98*, 1269-1281. DOI: https://doi.org/10.1016/j.neuron.2018.05.019

[31] Muller, L., Chavane, F., Reynolds, J., and Sejnowski, T.J. (2018). Cortical travelling waves: mechanisms and computational principles. *Nature Reviews Neuroscience, 19*, 255–268.

[32] Menceloglu, M., Grabowecky, M., Suzuki, S. (2020). Spectral-power associations reflect amplitude modulation and within-frequency interactions on the sub-second timescale and cross-frequency interactions on the seconds timescale. *PLoS ONE 15(5)*: e0228365. https://doi.org/10.1371/journal.pone.0228365

[33] Menceloglu, M., Grabowecky, M., Suzuki, S. (2020). EEG state-trajectory instability and speed reveal global rules of intrinsic spatiotemporal neural dynamics. *PLoS ONE 15(8)*: e0235744. https://doi.org/10.1371/journal.pone.0235744

[34] Menceloglu, M., Grabowecky, M., & Suzuki, S. (2021). Spatiotemporal dynamics of maximal and minimal EEG spectral power. *PLoS ONE 16(7)*: e0253813. https://doi.org/10.1371/journal.pone.0253813

[35] Menceloglu, M., Grabowecky, M., Suzuki, S. (2021). Probabilistic, entropy-maximizing control of large-scale neural synchronization. *PLoS ONE 16(4)*: e0249317. https://doi.org/10.1371/journal.pone.0249317

[36] Menceloglu, M., Grabowecky, M. & Suzuki, S. (2021). A phase-shifting anterior-posterior network organizes global phase relations. https://www.biorxiv.org/content/10.1101/2021.12.21.473764v1

[37] Delorme, A., & Makeig, S. (2004). EEGLAB: an open source toolbox for analysis of single-trial EEG dynamics including independent component analysis. *Journal of neuroscience methods*, *134*(1), 9-21.

[38] Lopez-Calderon, J., & Luck, S. J. (2014). ERPLAB: an open-source toolbox for the analysis of event-related potentials. *Frontiers in human neuroscience*, *8*, 213.

[39] Cottereau, B. R., Ales, J. M., & Norcia, A. M. (2015). How to use fMRI functional localizers to improve EEG/MEG source estimation. *Journal of Neuroscience Methods, 250*, 64-73.

[40] Nunez, P. L., Silbersten, R. B., Cadusch, P. J., Wijesinghe, R. S., Westdorp, A. F., & Srinivasan, R. (1994). A theoretical and experimental study of high resolution EEG based on surface Laplacians and cortical imaging. *Electroencephalography and Clinical Neurophysiology, 90*, 40-57.

[41] Tenke, C. E., & Kayser, J. (2012). Generator localization by current source density (CSD): Implications of volume conduction and field closure at intracranial and scalp resolutions. *Clinical Neurophysiology, 123*, 2328–2345.

[42] Cohen, M. X. (2015). Comparison of different spatial transformations applied to EEG data: a case study of error processing. *International Journal of Psychophysiology, 97*, 245-257.

[43] Nunez, P., & Srinivasan, R. (2006). *Electric fields of the brain: The neurophysics of EEG*. Oxford University Press.

[44] Hjorth, B. (1980). Source derivation simplifies topographical EEG interpretation. *American Journal of EEG Technology 20*, 121-132.

[45] Kayser, J., Tenke, C. E. (2006). Principal components analysis of Laplacian waveforms as a generic method for identifying ERP generator patterns: I. Evaluation with auditory oddball tasks. *Clinical Neurophysiology, 117*, 348-368.

[46] Cohen, M. X. (2014). *Analyzing Neural Time Series Data: Theory and Practice*, MIT Press.

[47] Perrin, F., Pernier, J., Bertrand, O., Giard, M. H., & Echallier, J. F. (1987). Mapping of scalp potentials by surface spline interpolation. *Electroencephalography and Clinical Neurophysiology, 66 (1)*, 75-81.

[48] Perrin, F., Pernier, J., Bertrand, O., & Echallier, J. F. (1989). Spherical splines for scalp potential and current density mapping. *Electroencephalography and Clinical Neurophysiology 72(2)*: 184-187.

[49] Perrin, F., Pernier, J., Bertrand, O., & Echallier, J. F. (1989). Corrigenda EEG 02274. *Electroencephalography and Clinical Neurophysiology 76*, 565.

[50] van Albada, S. J., & Robinson, P. A. (2013). Relationships between electroencephalographic spectral peaks across frequency bands. *Frontiers in Human Neuroscience, 7: 56* https://doi.org/10.3389/fnhum.2013.00056

[51] Chiang, A. K. I., Rennie, C. J., Robinson, P. A., van Albada, S. J., & Kerr, C. C. (2011). Age trends and sex differences of alpha rhythms including split alpha peaks. *Clinical Neurophysiology, 122*, 1505-1517.

[52] Donoghue, T., Haller, M., Peterson, E. J., Varma, P., Sebastian, P., Gao, R., Noto, T., Lara, A. H., Waliis, J. D., Knight, R. T., Shestyuk, A., & Voytek, B. (2020). Parameterizing neural power spectra into periodic and aperiodic components. *Nature Neuroscience, 23*, 1655-1665.

[53] He, B. J. (2014). Scale-free brain activity: past, present, and future. *Trends in Cognitive Sciences, 18(9)*, 480-487.

[54] Gao, R., Peterson, E. J., & Voytek, B. (2017). Inferring synaptic excitation/inhibition balance from field potentials. *Neuroimage, 158*, 70-78.

[55] Andreou, D, & Poli, R. (2016). Comparing EEG, its time-derivative and their joint use as features in a BCI for 2-D pointer control. 38th Annual International Conference of the IEEE Engineering in Medicine and Biology Society (EMBC), pp. 5853-5856, doi: 10.1109/EMBC.2016.7592059.

[56] Hess, R. F. & Snowden, R. J., (1992) Temporal properties of human visual filters: Number, shapes and spatial covariance, *Vision Research, 32*, 47-60.

[57] Lui, L. L., Bourne, J. A., Rosa, M. G. P. (2007). Spatial and temporal frequency selectivity of neurons in the middle temporal visual area of new world monkeys (Callithrix jacchus). *European Journal of Neuroscience, 25*, 1780-1792.

[58] Moon, J. Y., Lee, U., Blain-Moraes, S., and Mashour, G. A. (2015). General relationship of global topology, local dynamics, and directionality in large-scale brain networks. *PLoS Computational Biology,* 11: e1004225. DOI: 10.1371/journal.pcbi.1004225

[59] Tewarie, P., Hunt, B. A., O'Neill, G. C., Byrne, A., Aquino, K., Bauer, M., Mullinger, K. J., Coombes, S., & Brookes, M. J. (2019). Relationships between neuronal oscillatory amplitude and dynamic functional connectivity. *Cerebral Cortex, 29*, 2668-2681. DOI: 10.1093/cercor/bhy136

[60] Alexander, D. M., Jurica, P., Trengove, C., Nikolaev, A. R., Gepshtein, S., Zvyagintsev, M., Mathiak, K., Schulze-Bonhage, A., Ruescher, J., Ball, T., van Leeuwen, C. (2013). Traveling waves and trial averaging: the nature of single-trial and averaged brain responses in large-scale cortical signals. *NeuroImage, 73*, 95–112.

[61] Alamia, A. & VanRullen, R. (2019). Alpha oscillations and traveling waves: Signatures of predictive coding? *PLoS Biology, 17(10)*: e3000487. https://doi.org/10.1371/journal.pbio.3000487

[62] Ermentrout, G. B., & Kleinfeld, D. (2001). Traveling electrical waves in cortex: insights from phase dynamics and speculation on a computational role. *Neuron, 29*, 33-44.